RUPTURE PROCESS OF THE 2004 PARKFIELD EARTHQUAKE UTILIZING NEAR-FAULT SEISMIC RECORDS AND IMPLICATIONS FOR SHAKEMAP

Douglas Dreger and Ahyi Kim

Berkeley Seismology Laboratory
University of California Berkeley

Abstract

The September 28, 2004 Parkfield earthquake, arguably the best recorded earthquake ever, allows for detailed investigation of finite-source models, and their resolution. We have developed models using GPS and InSAR geodetic data, and CSMIP and USGS strong motion seismic waveforms independently and jointly. In order to focus on better resolved long wavelength features the seismic data was lowpass filtered at 0.5 Hz. We have investigated the sensitivity of the finite-source models due to station coverage, weighting and smoothing parameters, and seismic velocity structure. The resulting model is consistent with preliminary results using regional broadband and strong motion waveform data (e.g. Langbein et al., 2005; Dreger et al., 2005) as well as with higher frequency seismic waveform only inversions (e.g. Custódio et al., 2005; Liu et al., 2006). The scalar seismic moment was found to be 1.28e25 dyne cm (Mw6.0), the overall rupture length 25 km, the peak slip 58 cm, and the average rupture velocity 2.6 km/s. The rupture was predominantly unilateral to the NW with a small component to the SE. The obtained slip model was used to simulate 3D wave propagation taking into account the velocity contrast across the San Andreas Fault, and a narrow low-velocity fault zone. The results of this analysis suggest observed waveform complexity and amplitudes at stations located in the fault zone could be due to fault zone guided waves.

Introduction

On September 28, 2004 the long awaited Parkfield mainshock occurred 16 years past its expected due date, nearly a full cycle past the regular recurrence interval of 22 years. Fortunately the investment in geophysical monitoring of the region paid off as most systems were kept running. This foresight and persistence by the network operators has lead to the best near-fault geophysical data set of a moderate earthquake to date.

In this study we have developed kinematic finite-source models for the event using the local strong motion waveform data provided by CSMIP and NSMP, as well as coseismic GPS and InSAR deformation data. Independent models for each data set, as well as our preferred joint inversion model are presented.

In Dreger et al. (2005) the automated finite-source inversion method developed by Dreger and Kaverina (2000) was applied to regional broadband waveform data from CISN stations. The kinematic model in that study showed a rupture which nucleated near Gold Hill, and propagated 25 km unilaterally to the NW stopping at Middle Mountain, the opposite of the

1934 and 1966 Parkfield earthquakes. The kinematic model was used to simulate near-fault strong ground motions, and the largest motions were found to be NW of the epicenter. The updated CISN ShakeMap on the other hand shows a bimodal distribution in peak ground motions, where large amplitude motions are also located SE of the epicenter along the Cholame array (CH stations, Figure 1). Therefore an objective of our study is to understand the reason for the bimodal ground motion distribution to ascertain whether it is due to unaccounted for source process or possibly 3D wave propagation in the fault zone.

Data

Strong Motion Waveforms

We used horizontal records from 29 strong motion sites (Figure 1), which provided excellent azimuthal coverage of the ruptured fault. Some sites close to the fault were excluded because they exhibited waveform complexity indicative of fault zone guided wave propagation, which could not be modeled with the assumed 1D velocity model Green's functions.

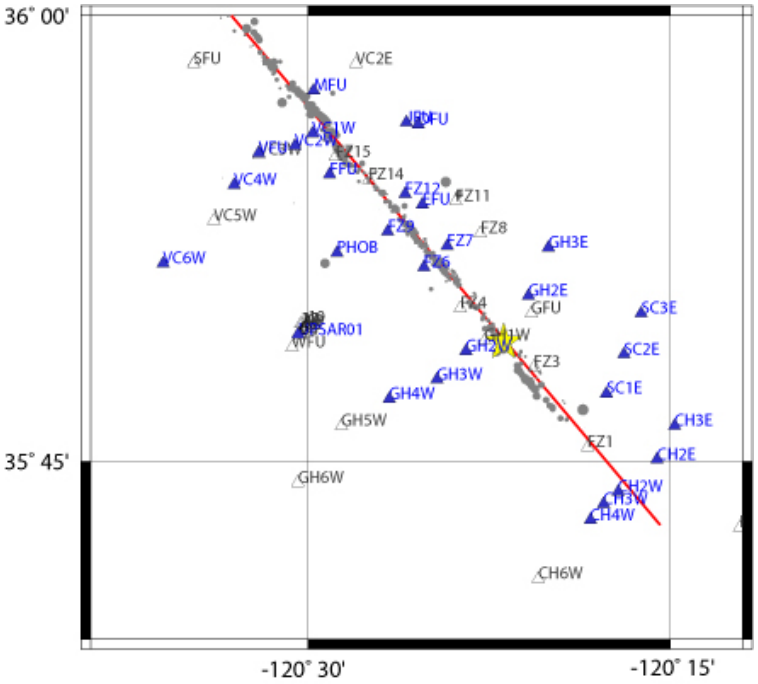

Figure 1. CSMIP and USGS strong motion stations. The filled triangles show the sites used to determine the kinematic source model. The star shows the epicenter and the gray circles background seismicity and aftershocks.

For example, Figure 2 compares north-south records from the CSMIP Gold Hill array (GH1W, GH2W and GH3W, Figure 1). It is evident that the GH1W record has an extended duration compared to the other two stations only a few km to the west. Since GH1W is close to the epicenter, and the faulting mechanism is a nearly vertical dipping, right-lateral strike-slip fault, the motions theoretically should be very small due to the radiation pattern, but as Figure 2 shows they are nearly the same amplitude as the more distant stations. The amplitude and extended duration is likely due to fault zone guided or trapped waves propagating within the low

velocity core of the San Andreas Fault (e.g. Korneev et al., 2003). In this report we will demonstrate with 3D finite-difference modeling that this is likely the case. In any event, for the inversion, it was necessary to exclude the waveforms at sites that exhibited this complexity because the method we employed could not account for guided wave propagation.

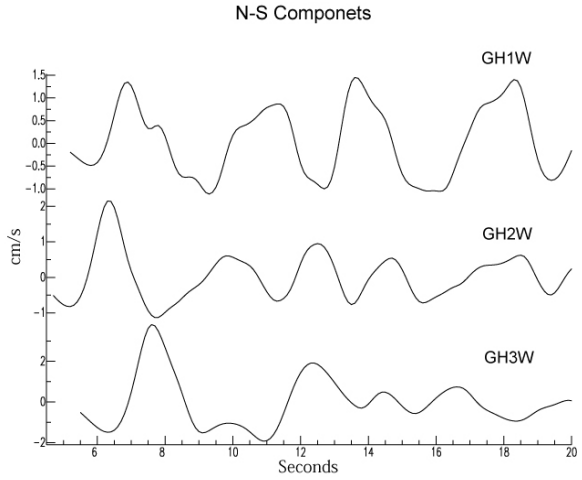

Figure 2. Comparison of N-S component velocity waveforms from stations of the Gold Hill array. GH1W is the site closest to the fault within the low velocity fault core (e.g. Korneev et al., 2000; 2003). This record has several cycles of large amplitude arrivals (actually extending beyond what is plotted). The other two stations located to the west of the fault outside the gouge region have simpler waveforms characterized by a primary initial S-wave pulse.

The waveforms were processed by integrating recorded acceleration to velocity, and lowpass filtering with an acausal Butterworth filter with a corner frequency of 0.5 Hz. The records were then resampled to 10 samples per second. The filtering was done in order to focus on getting a better resolved longer wavelength source process, and because the 1D velocity structures likely could not model high frequency wave propagation.

GPS Deformation

GPS deformation data was obtained from 1 second continuous GPS observations at 13 sites. To obtain the coseismic deformation the 1 second time series were averaged 10 minutes before the event and 2 to 10 minutes afterward. Because of the high sample rate data it is unlikely that much postseismic deformation signal is present in the GPS data set.

InSAR Deformation

The coseismic deformation from ENVISAT InSAR data was obtained from a pre event scene on 7/3/2003 and post event scene on 9/30/2004. We used the interferogram processed by Johanson et al. (2006) in which non-tectonic effects, especially atmospheric changes, and groundwater induced vertical motion were removed. Because the post-event scene is two days after the event there could be some postseismic signal present in the data.

Development of a Kinematic Rupture Model

Method

We use the method of Hartzell and Heaton (1983), which is the same method we used in developing our automated finite-source procedure (Dreger and Kaverina, 2000; Dreger et al., 2005). The multiple time window parameterization of this method allows for some variability in rupture velocity as well as variability in the dislocation rise time, and has the advantage of being a linear inversion for the slip distribution.

The fault model is parameterized as a 44 km length by 18 km width fault. The strike is 140 degrees and the dip is 89. The fault orientation was obtained by fitting the single fault plane to the aftershock distribution (Figure 1). The fault extends 29 km NW of the hypocenter and 15 km to the SE. The overall model dimension exceeds what is necessary to fit the data. The fault model is discretized with 792 1 km by 1 km subfaults.

We initially tested variable rake models, but found that the results were strike-slip, and therefore in subsequent modeling we assumed a constant rake of 180 degrees. Focal mechanisms reported in Thurber et al. (2006) for background seismicity and aftershocks support this assumption.

We allowed 12 time windows each with a dislocation rise time of 0.6 seconds with each subsequent time window offset by 0.3 seconds giving a total rise time range from 0.6 to 3.6 seconds. All 12 time windows yields 9504 free parameters though our subsequent sensitivity modeling revealed that most of the slip was contained in the first 6 time windows.

To stabilize the inversion we employ slip positivity using the non-negative least squares routine (Lawson. and Hanson 1974), spatial smoothing and moment minimization constraints. We examine the smoothing weight and data weighting parameter space to find the optimum solution with a trial and error approach.

Because we lowpass filtered the seismic waveform data at 0.5 Hz it is not necessary to use site amplification terms. Liu et al. (2006) used records from the Coalinga earthquake recorded at Parkfield stations to determine relative site amplification terms as a function of frequency. Some stations show broadband amplification, but most others show a frequency dependent site response. Generally their amplification factors for $f<0.5$ were relatively small, and the sites with the largest factors tended to be the fault zone sites we eliminated due to guided wave signatures in the waveforms.

Because the velocity differs across the fault (Michaels and Eberhart-Phillips, 1991; Michelini and McEvilly, 1991; Thurber et al., 2006) we performed inversions using both a single velocity structure as well as a two velocity model case. Our preferred inversion utilizes two 1D velocity models to represent the contrast across the fault. The velocity models after Liu et al., (2006) are shown in Table 2.

The use of simplified velocity structure can lead to artificial absolute time shifts between Green's functions and the observed records. Therefore we required that the observed first arriving S wave at each site be aligned with the S-wave arrival from the Green's function for the hypocenter following the approach of Wald et al. (1991). Table 1 lists the stations and the applied time shifts.

Independent Inversions

We performed inversions of each data set independently and the results of these inversions are compared in Figure 3. The results show some common features, namely that the rupture propagated from the hypocenter to the NW, and that the highest slip was located 10-20km northwest of the hypocenter. In general these results are consistent with those reported in Langbein et al. (2005) and Dreger et al. (2005), which utilized regional distance stations. However in detail the three models differ.

Seismic Waveform Inversion

The kinematic model obtained with only seismic waveform data (Figure 3a) shows some slip located close to the hypocenter; however the largest asperity is 10 to 20 km to the NW. The slip is generally found to be located below a depth of 5 km, and is shallower than 15 km. Slip shallower than 5 km in the model is not well constrained. This model also has some low levels of slip to the south of the hypocenter that is needed to fit the waveforms from the Cholame array. Thus, there is some indication of a slight bilateral rupture; however the rupture was principally unilateral to the NW. The best fit variance reduction for the seismic waveform data is 69.5%. The scalar seismic moment was found to be 1.35e+25 dyne cm (Mw6.05). Finally, we note that these results are consistent with what we obtained previously (e.g. Langbein et al., 2005; Dreger et al., 2005) with the regional seismic waveforms and near-fault GPS data.

Geodetic Inversion

The inversion results for the geodetic data also show shallow slip extending about 25 km NW of hypocenter. The GPS inversion (Figure 3b) tends to have slip concentrated in two asperities, one at the hypocenter and the other 10 to 20 km to the NW. The InSAR result (Figure 3c) on the other hand tends to have slip in a continuous band, though it is peaked at the two ends. Both inversions are consistent with the seismic result in terms of the overall rupture dimension, and the fact that the slip is shallower than 15 km. The two geodetic results also seem to have more significant SE-ward slip, which extends as much as 10 km to the SE. The best fit variance reductions for the two independent inversions were found to be 97.0% (GPS) and 74.8% (InSAR).

The relatively higher slip in the InSAR only model might be due to included postseismic deformation since the post-event scene is 2-days after the mainshock. The scalar seismic moment for the GPS inversion was found to be 1.25e+25 dyne cm (Mw6.03), and was 1.73e+25 (Mw6.12) for the InSAR inversion. The GPS scalar moment is about 7% less than the seismic model indicating that our coseismic estimates of GPS deformation are reasonable. The InSAR

scalar moment is about 28% higher than the seismic estimate indicating that some postseismic deformation may be included.

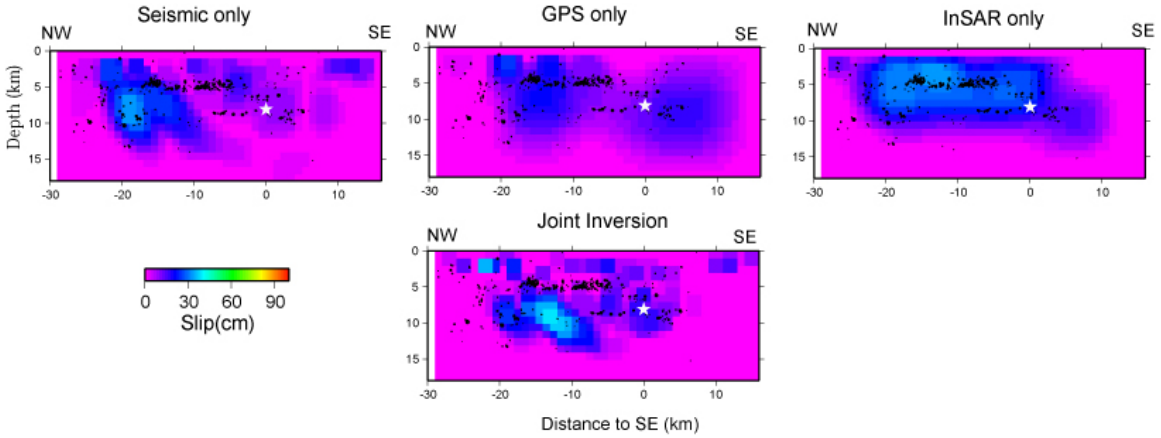

Figure 3. a) Seismic only inversion. b) GPS only inversion. c) InSAR only inversion. d) Joint inversion of all three data sets. The hypocenter is marked by the white star.

Joint Inversion

The preferred model, in which the three data sets were inverted simultaneously, is presented in Figure 3d. This model is consistent with our preliminary model with local and regional seismic and GPS data (Dreger et al., 2005) in that there are two primary asperities, one near the hypocenter, and the other 10-20km northwest of the hypocenter.

The slip in this model is also complementary (or anti-correlated) with the postseismic slip determined by Johanson et al. (2006), and is also complementary to the distribution of aftershocks. Most notable is the lack of slip in the region of the seismicity streak at 5 km depth. The slip shallower than 2 km depth is not well constrained. The scalar seismic moment in this model is 1.28e25 dyne-cm (Mw6.0) with a peak slip of 58cm.

Since different data sets with different numbers of observations are used in the joint inversion it is necessary to weight them relative to each other. This was done by generating a tradeoff plot in which the fit to the data was compared to the relative weight of each data set. In Figure 4a we show the weight of the InSAR+GPS data relative to the seismic waveform data. An inflection in the curves occurs at weight of 3000, where a larger weight would better fit the geodetic data at the detriment of the fit to the seismic waveforms. With a weight of 3000 the fit of all three data sets remains close to their respective best fits, and therefore this value is considered reasonable. Next, we assume the obtained data weight, and then find the smoothing weight again using a tradeoff curve (Figure 4b). Here we find the largest value of smoothing that still retains an acceptable level of fit to all data sets. Again we look for an inflection where there is a discernable change in the fit to the data. An optimal smoothing weight of 0.002 was found from the analysis.

The variance reductions for each data set in the joint inversion were less than obtained from each of the independent inversions as expected, however they remained high; 66.9% (seismic), 90.1% (GPS) and 54.7% (InSAR). The seismic waveform and GPS fits are very close

to their respective maxima, however the InSAR fit dropped by 20%. The joint inversion scalar moment is close to what was obtained in the seismic and GPS inversions, but substantially less than the InSAR result. Thus, it appears that the inversion is fitting the coseismic component of the InSAR observations leaving unmodeled the postseismic deformation.

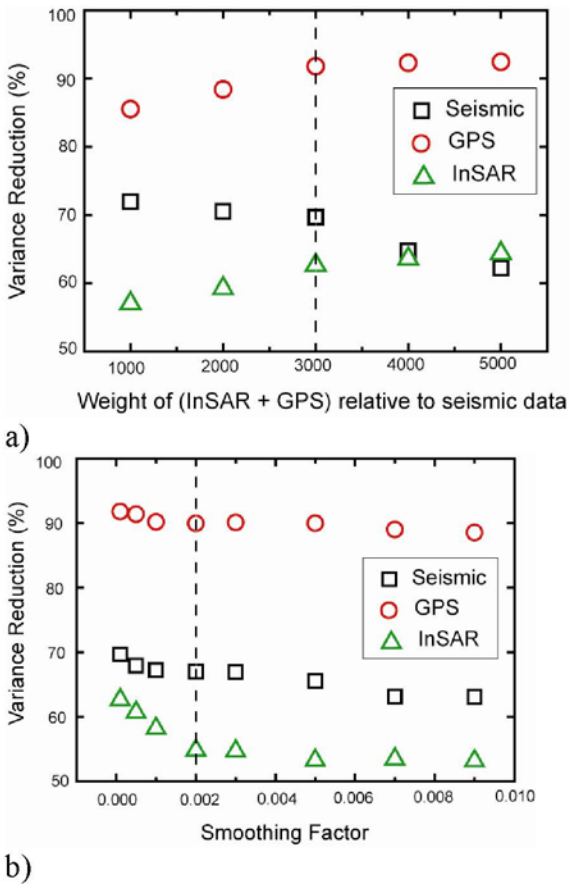

Figure 4. a) Weight of the InSAR+GPS data relative to the seismic waveform data vs. model fit. b) For the optimal weight the smoothing factor vs. model fit. In each case the preferred value is marked by the dashed line, which was chosen based on the point where there is a change in the slope of each curve.

We performed a series of inversions with seismic+GPS and seismic+GPS+InSAR to evaluate the effect of the InSAR data, and found that it provided additional constraint without dominating the inversion. Because the InSAR data provides substantially better coverage than either the GPS or the seismic sites we prefer to include it in the joint inversion.

The fit to the seismic waveforms as shown in Figure 5 is quite good. We included the waveforms from the Cholame array to investigate the possibility of SE-ward rupture. We can fit some of those stations (CH2E, CH3E, CH4W) very well; however there are problems at other stations located closer to the fault. For example we under predict CH2W. The CH2W waveforms are more complex with several additional cycles of motion. Although this is a fault zone signature, we left this station in the inversion to specifically test the hypothesis of SE-ward rupture. The small amount of SE-ward slip in the preferred model is needed to explain the Cholame records in general, but it is not sufficient to describe the high amplitudes and waveform

complexity. The site factor determined by Liu et al. (2006) for this station is only 1.12 so not using site factors do not appear to be the cause of the misfit.

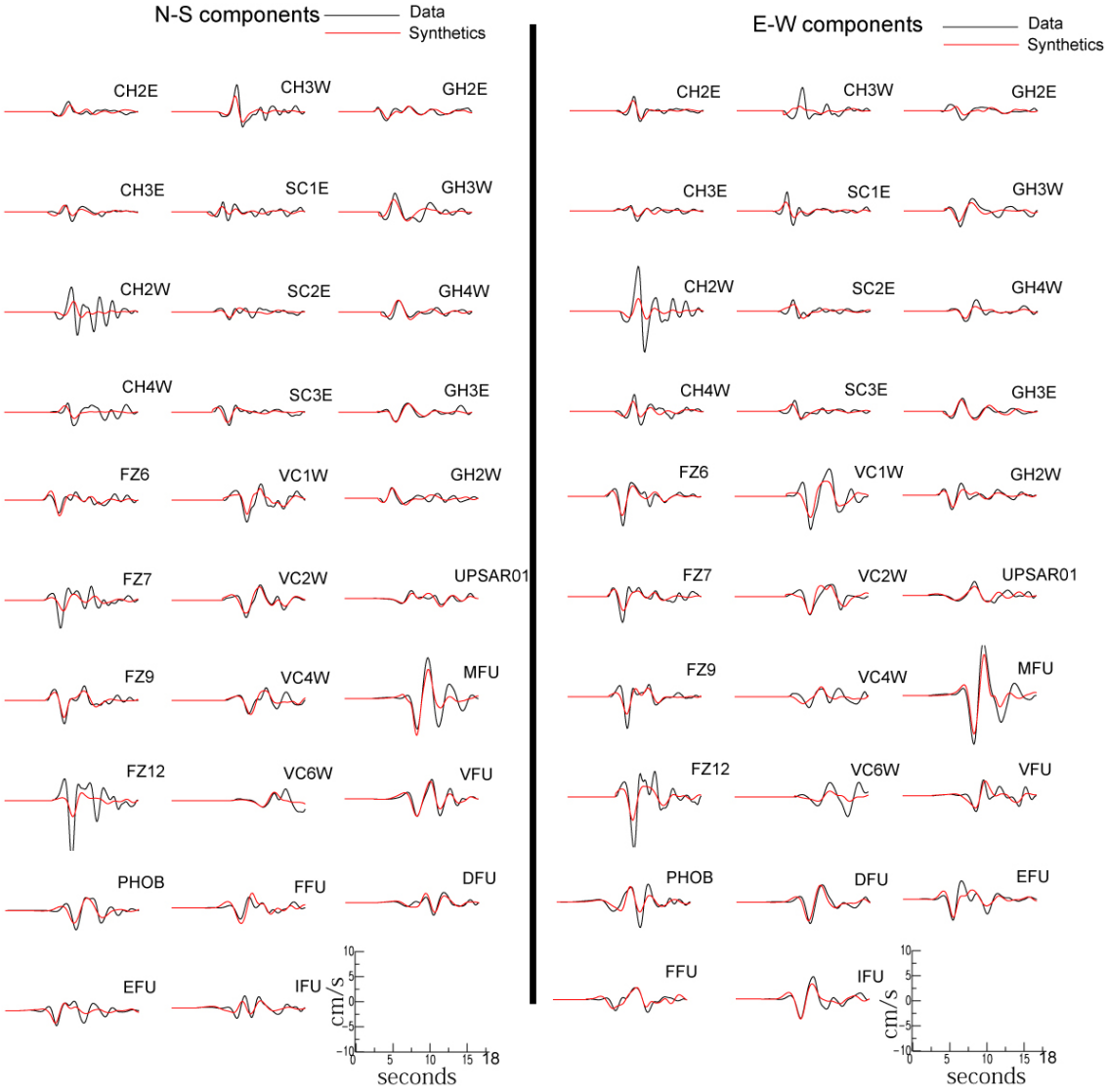

Figure 5. Comparison of data (black) and synthetics (red) for the joint inversion. The left panel shows the NS component and the right panel the EW component. The amplitude scale is in cm/s and the time scale shows seconds.

Although the seismic only inversion fits the Cholame stations better they are still fit worse than other stations used in the inversion. Another problematic station is FZ12, which is located close to the main trace of the SAF (Figure 1). For this station we only fit half of the amplitude. Interestingly we fit the nearby EFU records very well. In the next section we present 3D simulations that take into account the velocity contrast across the fault as well as a low velocity fault zone that produces the observed waveform complexity and extended duration at sites located within the fault zone. Based on that analysis we believe that the elevated amplitudes

at the near-fault stations of the Cholame array and also the FZ1 site (not used in the inversion due to fault zone waveform complexity) is due to fault zone guided wave effects.

The fit to the geodetic data is also very good. Figure 6 shows the fit to the GPS data, and Figure 7 shows the fit to the InSAR data. This plot also shows that the assumed fault geometry based on fitting the plane to the seismicity is consistent with the differential deformation imaged by InSAR.

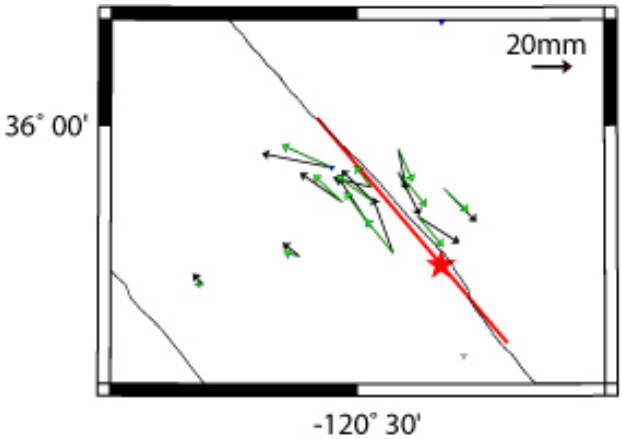

Figure 6. Comparison of observed (black) and simulated (green) GPS deformation. The hypocenter is shown by the star and surface projection of the fault plane by the red line.

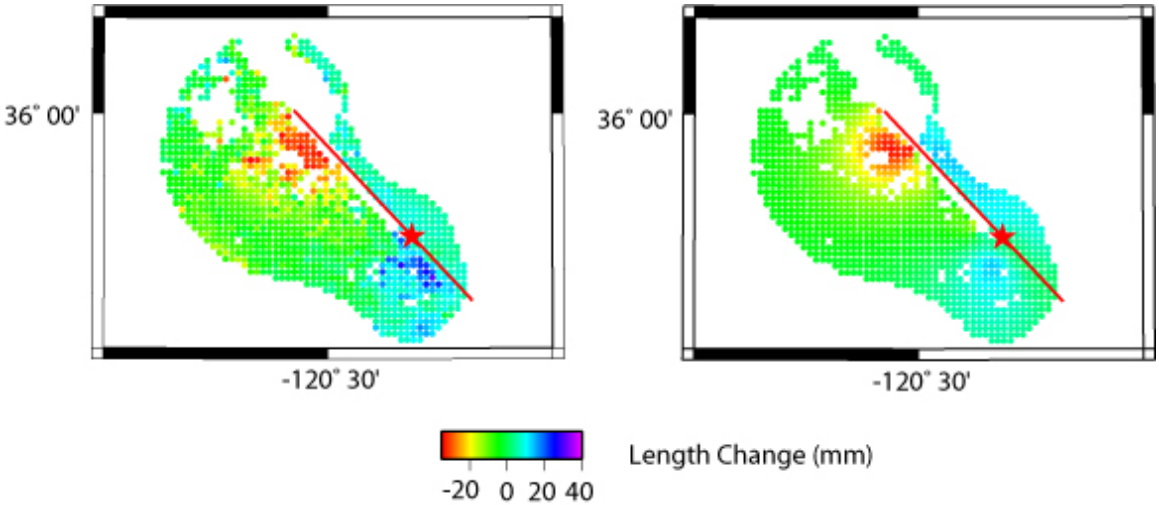

Figure 7. Observed line length change (left) is compared to predictions (right) for the preferred finite-source model. This image is for an ascending orbit. The data was edited by Johanson et al. (2006) to remove decorrelated pixels due to atmospheric disturbance.

The best average rupture velocity was found to be 2.6km/s (Figure 8). We did examine the possibility of super-shear rupture, but did not find a significant improvement in fit. Fletcher and Spudich (2006) investigated the data from the UPSAR array where they were able to determine the slowness and azimuth of the incident wavefield and were able to map the rupture

propagation. They concluded that the rupture was sub-shear. The results of Liu et al. (2006) show a highly variable rupture velocity that is on average 2.6 km/s with a maximum of 3.3 km/s.

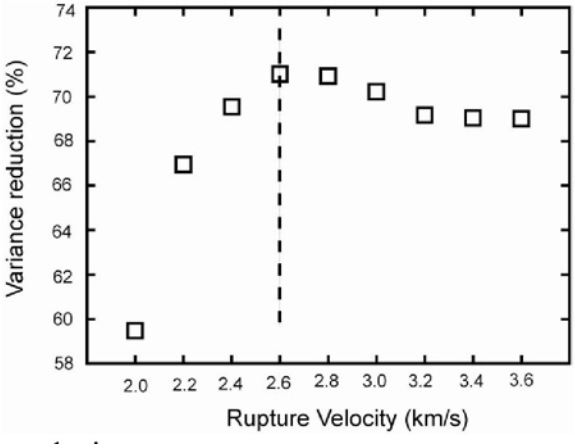

Figure 8. Fit vs. rupture velocity.

The bulk of the slip (93%) occurs in the first 6 time windows. Although some slip occurs in later time windows an examination of the synthetic waveforms indicated that it did not significantly affect the fit to the data, and that it was likely an artifact due to the mapping of propagation effects into the source. The first 6 time windows allow a range in rise time from 0.6 to 2.1 seconds, and we found that the average rise time during the rupture was 1.6 seconds.

Our preferred model compares favorably with the results of Custódio et al. (2005) and Liu et al. (2006). In those studies they used higher frequency waves (1 Hz) and consequently recovered models with shorter wavelength heterogeneity than in our model. They used a non-linear inversion for the slip trigger time and rise time, and reported that the rupture velocity is highly variable, but on average 2.6 km/s, which agrees with our result. They also developed multiple models for different station configurations (Custódio et al. 2005), and different random seeds (Liu et al. 2006), and from those models they obtained average slip models. Our model agrees very well with their average models in terms of the slip distribution. In fact, it is remarkable how similar they are considering the differences in linear vs. non-linear inversions, and their use of only seismic waveform data compared to our use of seismic and geodetic data. One major difference though is that in their models the peak slip is located at the hypocenter asperity, whereas in our model it is in the NW asperity. The similarity in the models as well as the complementary nature of coseismic slip with aftershock seismicity and postseismic deformation (Johanson et al., 2006) suggests the obtained slip model is robust.

Three Dimensional Fault Structure Effects on Ground Motions

There is a pronounced velocity contrast across the San Andreas Fault along the Parkfield segment (Michaels and Eberhart-Phillips, 1991; Michelini and McEvilly, Thurber et al., 2006). There is also evidence of a low velocity fault zone from the analysis of fault zone guided waves (Korneev et al., 2003). Korneev et al. (2003) were able to model the fault zone guided waves using a 200m wide fault zone extending to a depth of 8 km. The fault zone at Parkfield is wide as evidenced by mapped surface faults and where surface slip and creep occurred in the 1966 and

the 2004 Parkfield earthquakes (e.g. Langbein et al., 2005). For example the southwest fault zone likely marks the western extent of the San Andreas Fault system along the Parkfield segment, indicating that the fault zone is on the order of 1 km wide. The 3D model images of Thurber et al. (2006) show a fairly sharp contrast in the northern 2/3 of the fault segment in which velocities are faster on the SW side of the fault. In the vicinity of Gold Hill and southward to the Cholame array there is a 2-3 km wide low velocity zone adjacent to the plotted seismicity that extends from 5 km to about 15 km depth.

We used a 3D elastic finite-difference code, e3d (Larsen and Schultz, 1995), to simulate three-component velocity wavefields for a variety of fault models using a finite-source model derived from the preferred model described above. Simulations were performed using a single 1D structure, two 1D structures on opposite sides of the fault, and finally a sandwiched narrow low velocity zone. In order to generate synthetic records comparable to the fault zone station observations in terms of relative amplitude and duration we needed a low velocity fault zone 750m wide.

For purposes of simplifying the source parameterization we did not use the finite-source model exactly as determined. Although we did use the exact slip distribution, and the constant rupture velocity of 2.6 km/s, we did not use the multiple time window parameterizations for the slip time history. Instead we assumed a constant slip velocity of 80 cm/s and divided the slip at each point in the fault model by this value to obtain the local rise time. The local rise time was then used to define a local Gaussian shaped slip velocity function. Although the model used is not exactly the same as obtained from the inversion it does approximate the kinematic rupture process well, and is sufficient for evaluating 3D velocity structure effects on the near-fault wavefield.

The finite-difference model had dimensions of 80 km in the fault-parallel direction, 50 km in the fault perpendicular direction and 40 km in depth. The fault was centered in the grid. The grid discretization was 250m. The various simulations had minimum shear velocities of 1.5 and 1.0 km/s, and therefore the maximum frequency without significant grid dispersion effects is 0.75 and 0.5 Hz assuming 8 grid points per minimum wavelength.

In Figure 9 we compare results for stations of the Gold Hill array for a 1D reference run, and the 3D model that includes a 750m 1.0 km/s low velocity fault zone. The synthetics were low pass filtered with a corner frequency of 0.5 Hz.

This simulation very nicely illustrates the transition from complex fault zone time histories to simpler impulsive time histories at sites away from the fault, outside the low-velocity zone. Additionally the simulation shows that peak amplitude of the 3D synthetics at GH1W is 3 times higher than the near-nodal 1D reference run synthetics. In fact, the fault zone amplification effect can be greater than this. Differences in local site effects can compound the amplification at fault zone sites. Although the simulated GH1W record is similar to the observations in Figure 2 the simulated duration and period of the fault zone guided waves is not correct. These are a function of the fault zone width and the velocity in the fault zone. It would be possible to obtain better agreement with the observations by considering lower fault zone velocities, though that

would require increasing the resolution of the finite-difference calculation to maintain the same maximum frequency. We plan to do this in future work.

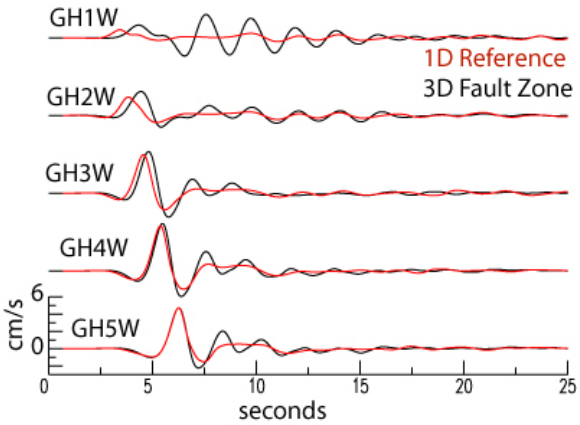

Figure 9. N-S component velocity synthetics for the Gold Hill array. The synthetics were computed with the preferred slip model, and a 3D fault model with a 750m gouge zone.

As shown previously we were able to fit the southern stations of the Cholame array quite well. Stations CH2E, CH3E, CH3W and CH4W are well modeled with fit comparable to that of other stations. Standing out is CH2W, which has a waveform with considerably more complexity and duration. 3D finite-difference synthetics for the Cholame array have the same behavior as the Gold Hill array shown in Figure 9, and therefore it seems that while a small component of southward slip is needed to fit the CH data, as shown above and by Liu et al. (2006), the large amplitudes observed at CH2W and FZ1 are most likely due to the combined effect of 3D fault zone guided waves and local site amplification.

The finite-difference results indicate that 3D fault zone wave propagation has a significant effect, and should be considered when inverting for high resolution images of the rupture process. Of course in order to do this requires a well constrained 3D geologic and velocity model. We will investigate the effect of 3D Green's functions on kinematic source inversions in future work.

Implications for ShakeMap

In Dreger et al. (2005) it has been shown that automated and rapidly reviewed finite-source information can greatly improve near-fault strong shaking estimates in cases where direct observations are not available. This was made clear in the ShakeMap response for the San Simeon earthquake (Figure 10), where the initial ShakeMap failed to portray the high level of shaking to the SE of the event near the towns of Paso Robles and Templeton. The ShakeMap taking the finite-fault rupture extent into account greatly improved the characterization of strong shaking in those areas. The question is how well resolved is a finite-source model obtained with regional distance data?

It is not expected that a finite-source model derived from a handful of regional distance (3 to 300 km) seismic stations would be comparable in detail with the results presented in this

report. Nevertheless, it is important to make this comparison to evaluate how well the regional distance approach does in characterizing slip. Figure 11 compares these two cases. The preferred joint inversion model obtained in this study is considered "truth" since it utilized many more stations at much closer distances, as well as including geodetic data. The regional model represents what can be obtained quickly after the occurrence of an event. As Figure 11 shows the two models do differ, which is not surprising, but it is also clear that they have many similar features such as the rupture extent, the depth range of rupture, the peak-slip and the scalar seismic moment. The slip in both models is focused into two asperities, one near the hypocenter and the other 10 to 20 km to the NW. This comparison shows that while the regional case is limited in its resolution of details of the source the obtained model is sufficient for purposes of including finite-source information in ShakeMap.

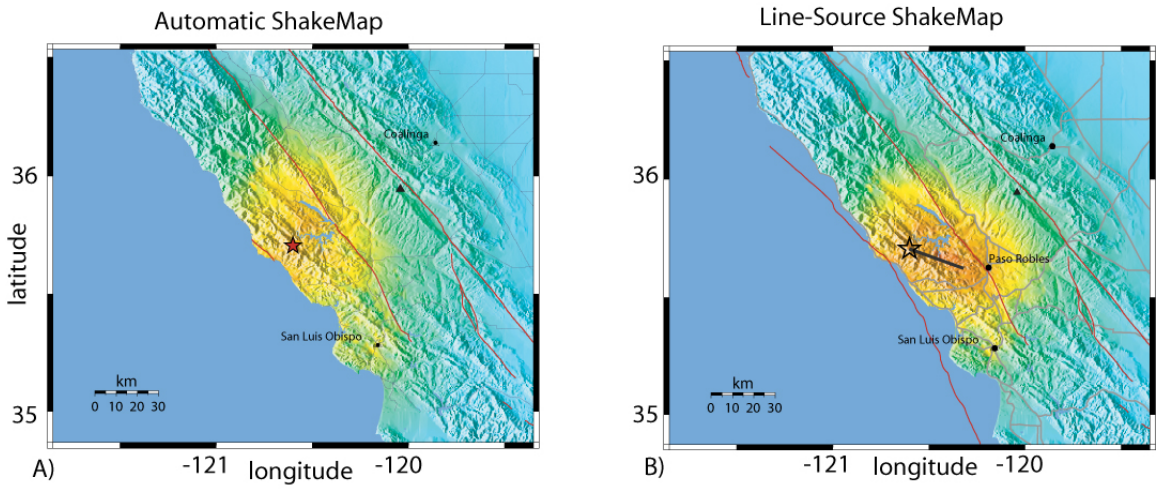

PERCEIVED SHAKING	Not felt	Weak	Light	Moderate	Strong	Very strong	Severe	Violent	Extreme
POTENTIAL DAMAGE	none	none	none	Very light	Light	Moderate	Moderate/Heavy	Heavy	Very Heavy
PEAK ACC.(%g)	<.17	.17-1.4	1.4-3.9	3.9-9.2	9.2-18	18-34	34-65	65-124	>124
PEAK VEL.(cm/s)	<0.1	0.1-1.1	1.1-3.4	3.4-8.1	8.1-16	16-31	31-60	60-116	>116
INSTRUMENTAL INTENSITY	I	II-III	IV	V	VI	VII	VIII	IX	X+

Figure 10. Comparison of (a) initial automatic ShakeMap with one that takes the rupture length determined from rapid finite-source inversion into account (b). The red star shows the epicenter, and the black line shows the extent of rupture. Note that there are no near-fault stations contributing to either map. In fact, the closest contributing stations was 55 km away. The map on the right was found to agree well with a map generated a few days after the event, which took into account the observed motions at several near fault sites (e.g. Dreger et al., 2005).

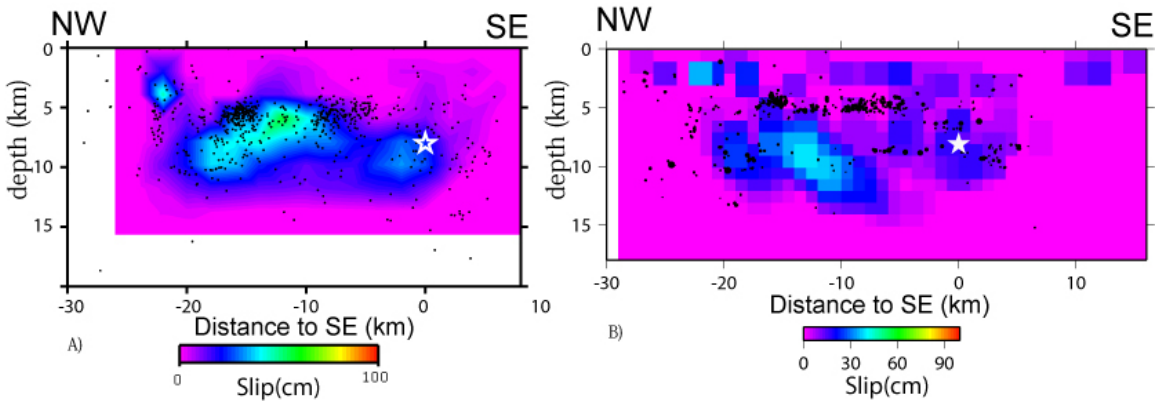

Figure 11. (a) Slip model obtained by inverting 9 three-component, regional distance displacement seismograms. This model was presented at the 2005 SSA meeting. (b) Preferred slip model based on the inversion of 29 two-component, near-fault velocity records, 13 GPS vectors, and InSAR deformation data.

Conclusions

We have developed kinematic finite-source models for the 2004 Mw6.0 Parkfield earthquake using the strong motion data collected by the California Geologic Survey CSMIP program. In addition, to these data we added strong motion records from the USGS NSMP and also GPS and InSAR geodetic data. A combined inversion of the three data sets produces the most constrained results. We find that the preferred slip model is consistent with our previous models obtained by inverting regional distance waveform data (e.g. Langbein et al., 2005; Dreger et al., 2005). This is a very positive result as it demonstrates that the automated regional distance finite-source method developed by Dreger and Kaverina (2000) is capable of recovering the kinematic finite-source rupture process with reasonably high resolution.

As shown by Dreger and Kaverina (2000) for the Mw7.1 Hector Mine earthquake and Dreger et al. (2005) for the Mw6.5 San Simeon earthquake rapidly determined fault slip models may be used to help constrain the level of near-fault strong shaking. In the case of the San Simeon earthquake the finite-source information, namely the length of the ruptured fault was instrumental in accurately characterizing strong shaking levels the day of the earthquake. Subsequently when a few near-event strong motion records became available the ShakeMap using the finite-source information was found to be consistent with the observations.

We incorporated 9 stations located SE of the epicenter in the inversion to try to resolve possible SE-ward rupture since elevated peak ground motions (Shakal et al., 2006) in this region suggest bilateral rupture. The results of our inversions (the seismic only and joint inversion) indicate that there was a small amount of SE-ward rupture, but that overall the 2004 Parkfield earthquake ruptured unilaterally to the NW.

We used our derived slip model to simulate the 3D wavefield for a fault model with an across-fault velocity contrast with a sandwiched low velocity zone. The results show that fault zone guided waves develop in this narrow zone greatly amplifying peak ground motions and producing complex multi-cycle waveforms. Based on this result we conclude that the elevated

motions SE of the epicenter at FZ1, at some sites of the Cholame array, and other sites located close to the fault are in part due to this 3D wave propagation effect.

The implications of this study for ShakeMap is two-fold. First, the similarity between the regional and near-fault finite-source models indicates that an automated regional distance approach is capable of producing reliable results for the rupture dimension and slip distribution. For both the San Simeon and Parkfield earthquakes including rupture length information (from aftershocks in the case of Parkfield) improved the ground motion characterization of ShakeMap. Second, the finite-difference simulation results indicate that near-fault motions can be affected by 3D fault structure. This is something that cannot easily be incorporated in an automated approach. It is therefore necessary to keep in mind that lateral velocity contrasts and fault zone low velocity can significantly increase the level of near-fault ground motions.

References

Custódio S., P. Liu, and R. J. Archuleta (2005). 2004 Mw6.0 Parkfield, California, earthquake: Inversion of near-source ground motion using multiple datasets, *Geophys. Res. Lett.,* 32, L23312, doi:10.1029/2005GL024417.

Dreger, D. S., L. Gee, P. Lombard, M. H. Murray, and B. Romanowicz (2005). Rapid Finite-Source Analysis and Near-Fault Strong Ground Motions – Application to the 2003 Mw6.5 San Simeon and 2004 Mw6.0 Parkfield Earthquakes, *Seismo. Res. Lett.* 76, 40-48.

Dreger, D., and A. Kaverina (2000). Seismic remote sensing for the earthquake source process and near-source strong shaking: A case study of the October 16, 1999 Hector Mine earthquake, Geophys. Res. Lett., 27, 1941-1944.

Eberhart-Phillips, D., and A.J. Michael, 1993, Three-dimensional velocity structure and seismicity in the Parkfield region, central California, J. Geophys. Res., 98, 15,737-15,758.

Fletcher, J. B., P. Spudich, and L. M. Baker (2006). Rupture propagation of the 2004 Parkfield earthquake from observations at the UPSAR array, *submitted to BSSA special issue on the Parkfield earthquake.*

Hartzell, S. H., and T. H. Heaton (1983) Inversion of strong ground motion and teleseismic waveform data for the fault rupture history of the 1979 Imperial Valley, California, earthquake, Bull. Seism. Soc. Am., 73, 1553-1583.

Johanson, I. A., E. J. Fielding, F. Rolandone, and R. Bürgmann (2006). Coseismic and postseismic slip of the 2004 Parkfield earthquake from space-geodetic data, *Bull. Seism. Soc. Am.,* 96, S269-S282.

Korneev, V. A., R. M. Nadeau, and T. V. McEvilly (2003). Seismological studies at Parkfield IX: Fault zone imaging using guided wave attenuation, Bull. Seism. Soc. Am., 93, 1415-1426.

Langbein, J., R. Borcherdt, D. Dreger, J. Fletcher, J. L. Hardebeck, M. Hellweg, C. Ji, M. Johnston,J. R. Murray, R. Nadeau, M. J. Rymer, J. A. Treiman (2005). Preliminary Report on the 28 September 2004, M 6.0 Parkfield, California Earthquake, *Seismo. Res. Lett.* 76, 10-26.

Larsen, S., and C. A. Schultz (1995). ELAS3D: 2D/3D elastic finite-difference wave propagation code, Technical Report No. UCRL-MA-121792, 19pp.

Lawson, C. L. and R. J. Hanson (1974) Solving Least Squares Problems, Prentice Hall, Englewood Clioes, New Jersey.

Lui, P., S. Custódio, and R. J. Archuleta (2006). Kinematic inversion of the 2004 Mw6.0 Parkfield earthquake including site effects, *Bull. Seism. Soc. Am.,* 96, S143-S158.

Michael, A. J., and D. Eberhart-Phillips (1991). Relationships between fault behavior, subsurface geology, and three-dimensional velocity models, Science, 253, 651-654.

Michelini, A., and T. V. McEvilly (1991). Seismological studies at Parkfield, part I: Simultaneous inversion for velocity structure and hypocenters using cubic B-splines parameterization, *Bull. Seism. Soc. Am.,* 81, 524-552.

Shakal, A., H. Haddadi, V. Graizer, K. Lin, and M. Huang (2006). Some key features of the strong-motion data from the M6.0 Parkfield, California, earthquake of 28 September 2004, *Bull. Seism. Soc. Am.,* 96, S90-S118.

Thurber, C., H. Zhang, F. Waldhauser, J. Hardebeck, A. Michaels, and D. Eberhart-Phillips (2006). Three-dimensional compressional wavespeed model, earthquake relocations, and focal mechanisms for the Parkfield, California, region, *Bull. Seism. Soc. Am.,* 96, S38-S49.

Wald, D. J., T. H. Heaton, and D. V. Helmberger (1991). Rupture model of the 1989 Loma Prieta earthquake from the inversion of strong motion and broadband teleseismic data, *Bull. Seism. Soc. Am.,*, 81 1540-1572.

Table 1: Station Locations and Applied Time Shifts

station	lat	lon	time shift (s)	station	lat	lon	time shift (s)
CH2E	35.751	-120.259	1.2	FZ9	35.879	-120.445	1.6
CH3E	35.770	-120.247	1.2	FZ12	35.900	-120.433	1.8
CH2W	35.733	-120.286	1.6	UPSAR01	35.821	-120.507	1.3
CH3W	35.726	-120.296	1.0	PHOB	35.867	-120.048	2.0
CH4W	35.717	-120.305	1.1	EFU	35.894	-120.421	0.4
SC1E	35.788	-120.294	0.9	FFU	35.911	-120.486	0.2
SC2E	35.810	-120.282	1.9	DFU	35.939	-120.425	2.4
SC3E	35.833	-120.27	1.2	JFU	35.939	-120.432	0.8
GH2E	35.842	-120.348	1.8	MFU	35.956	-120.496	0.1
GH3E	35.870	-120.334	1.8	VC1W	35.934	-120.497	0.8
GH2W	35.812	-120.391	1.8	VC2W	35.927	-120.509	0.8
GH3W	35.796	-120.411	1.8	VC4W	35.905	-120.551	1.3
GH4W	35.785	-120.444	1.7	VC6W	35.861	-120.600	1.2
FZ6	35.859	-120.42	1.9	VFU	35.922	-120.534	0.3
FZ7	35.871	-120.404	2.0				

Table 2: 1D Velocity Models

SW of the Fault						NE of the Fault					
Thickness (km)	Vp (km/s)	Vs (km/s)	density (kg/m^3)	Qp	Qs	Thickness (km)	Vp (km/s)	Vs (km/s)	density (kg/m^3)	Qp	Qs
1.0	1.9	1.0	2000	70	35	0.7	2.0	1.1	2000	70	35
1.0	3.4	1.7	2300	270	160	0.7	3.8	2.2	2300	300	180
1.0	4.6	2.4	2300	450	260	0.6	4.3	2.4	2300	340	190
1.0	5.1	3.1	2700	500	300	1.6	4.8	2.7	2300	450	250
1.4	5.6	3.6	2700	550	350	4.0	5.3	3.1	2500	500	300
13.3	6.3	3.6	2800	600	350	6.7	5.8	3.3	2700	550	300
∞	6.8	3.6	2800	680	360	6.2	6.2	3.8	2800	600	350
						4.1	6.8	3.8	2800	650	350
						∞	7.0	4.0	2800	700	400